$$F(a) = \sum_x \sum_y \left[a\, t_1(x, y) + \frac{1-a}{4} t_2(x, y) - t_3(x, y) \right]^2. \qquad \text{Eq. A16}$$

Setting the first derivative of F(a) to zero, parameter a is obtained as:

$$a = \frac{\sum_x \sum_y (t_3 - t_2/4)(t_1 - t_2/4)}{\sum_x \sum_y (t_1 - t_2/4)^2}. \qquad \text{Eq. A17}$$

Once parameter a is obtained, parameter b is calculated via Equation A8.

REFERENCES

1. Blau M, Nagler W, Bender MA. Fluorine-18: a new isotope for bone scanning. *J Nucl Med* 1962;3:332–334.
2. Anger HO, Van Dyke D, Gottschalk A, Yano Y, Schaer LR. The scintillation camera in diagnosis and research. *Nucleonics* 1965;23:57–62.
3. Van Dyke D, Anger HO, Yano Y, Bozzini C. Bone blood flow shown with F-18 and the positron camera. *Am J Physiol* 1965;209:65–70.
4. Reivich M, Kuhl D, Wolf A, et al. The [^{18}F]fluorodeoxyglucose method for measurement of local cerebral glucose utilization in man. *Circ Res* 1979;44:127–137.
5. Strauss LG, Conti PS. The applications of PET in clinical oncology. *J Nucl Med* 1991;32:623–648.
6. Coleman RE, Hoffman JM, Hanson MW, Sostman HD, Schold SC. Clinical application of PET for the evaluation of brain tumors. *J Nucl Med* 1991;32:616–622.
7. Burt RW, Perkins OW, Oppenheim BE, et al. Direct comparison of fluorine-18-FDG SPECT, fluorine-18-FDG PET and rest thallium-201 SPECT for detection of myocardial viability. *J Nucl Med* 1995;36:176–179.
8. Martin WH, Delbeke D, Patton JA, et al. FDG-SPECT: Correlation with FDG-PET. *J Nucl Med* 1995;36:988–995.
9. Delbeke D, Videlefsky S, Patton JA, et al. Rest myocardial perfusion/metabolism imaging using simultaneous dual-isotope acquisition SPECT with technetium-99m-MIBI/fluorine-18-FDG. *J Nucl Med* 1995;36:2110–2119.
10. Leichner PK, Morgan HT, Holdeman KP, et al. SPECT imaging of fluorine-18. *J Nucl Med* 1995;36:1472–1475.
11. Lange K, Carson R. EM reconstruction algorithms for emission and transmission tomography. *J Comput Assist Tomogr* 1984;8:306–316.
12. Zeng GL, Gullberg GT, Tsui BMW, Terry JA. Three-dimensional iterative reconstruction algorithms with attenuation and geometric point response correction. *IEEE Trans Nucl Sci* 1991;38:693–702.
13. Zeng GL, Gullberg GT. Frequency domain correction of the three-dimensional geometric point response function in SPECT imaging. *IEEE Trans Nucl Sci* 1992;39:1444–1453.
14. Liang Z, Jaszczak RJ, Turkington TG, Gilland DR, Coleman RE. Simultaneous compensation for attenuation, scatter and detector response of SPECT reconstruction in three dimensions. *Phys Med Biol* 1992:587–603.
15. Frey EC, Tsui BMW. A practical method for incorporating scatter in a projector-backprojector for accurate scatter compensation in SPECT. *IEEE Trans Nucl Sci* 1993;40:294–299.
16. Zeng GT, Hsieh YL, Gullberg GT. A rotating and warping projector-backprojector pair for fan-beam and cone-beam iterative algorithms. *IEEE Trans Nucl Sci* 1994;41:2807–2811.
17. Wallis JW, Miller TR, Miller MM, Hamill J. Rapid 3-D projection in iterative reconstruction using Gaussian diffusion [Abstract]. *J Nucl Med* 1996;37:63P.
18. McCarthy AW, Miller MI. Maximum likelihood SPECT in clinical computation times using mesh-connected parallel computers. *IEEE Trans Med Imag* 1991;10:426–436.
19. Di Bella EVR, Trisjono F, Zeng GL. Recursive blur models for SPECT depth-dependent response [Abstract]. *J Nucl Med* 1996;37:153P.
20. Hudson HM, Larkin RS. Accelerated EM reconstruction using ordered subsets of projection data. *IEEE Trans Med Imag* 1994;13:601–609.
21. Wolberg G. *Digital image warping.* Los Alamitos, CA: IEEE Computer Society Press; 1990.
22. Di Bella EVR, Barclay AB, Eisner RL, Schafer RW. A comparison of rotation-based methods for iterative reconstruction algorithm. *IEEE Trans Nucl Sci* 1996;43:3370–3376.
23. Metz CE, Atkins FB, Beck RN. The geometric transfer function component for scintillation camera collimators with straight parallel holes. *Phys Med Biol* 1980;25:1059–1070.
24. King MA, Glick SJ, Penney BC, Schwinger RB, Doherty PW. Interactive visual optimization of SPECT prereconstruction filtering. *J Nucl Med* 1987;28:1192–1198.
25. Hawkins WG, Yang NC, Leichner PK. Validation of the circular harmonic transform (CHT) algorithm for quantitative SPECT. *J Nucl Med* 1991;32:141–150.
26. Pan X, Metz CE, Chen CT. A class of analytical methods that compensate for attenuation and spatially-variant resolution in 2D SPECT. *IEEE Trans Nucl Sci* 1996;43:2244–2254.
27. Byrne CL. Block-iterative methods for image reconstruction from projections. *IEEE Trans Image Proc* 1996;5:792–794.

Pinhole SPECT Imaging in Normal and Morbid Ankles

Yong-Whee Bahk, Soo-Kyo Chung, Young-Ha Park, Sung-Hoon Kim and Hyoung-Koo Lee

Department of Radiology, Samsung Cheil Hospital, Seoul; and Department of Nuclear Medicine, Catholic University Medical College Hospitals, Seoul and Suwon, Korea

Pinhole SPECT can generate sectional nuclear images of a normal and morbid ankle and hindfoot with remarkably enhanced resolution by portraying the topography and pathological alterations in great detail. **Methods:** Pinhole SPECT was performed using a commercially available single-head, rotating gamma camera system by replacing the parallel-hole collimator used for planar SPECT with a pinhole collimator. The images were reconstructed in the same way as in planar SPECT by using the filtered back-projection algorithm and a Butterworth filter. First, we compared the scan resolution between the planar and pinhole SPECT images of a thyroid phantom and a normal ankle and hindfoot by working out pinhole SPECT anatomy with CT validation. Second, the clinical usefulness was assessed in one case each of fracture, reflex sympathetic dystrophy syndrome and rheumatoid arthritis of the ankle with radiographic correlation. The resolution of the pinhole SPECT and planar pinhole images was compared for these diseases. **Results:** The resolution of the pinhole SPECT of a thyroid phantom and of a normal ankle and hindfoot was significantly enhanced compared to the planar SPECT although image distortion was seen in the periphery of the field-of-view. The pinhole SPECT resolution was such that most of the anatomical landmarks were sharply delineated in the ankle and hindfoot and some useful diagnostic signs in the diseased ankle were visible. **Conclusion:** Pinhole SPECT can be performed using a single-head gamma camera system and filtered back-projection algorithm. It generates sectional scan images of both normal and morbid ankle and hindfoot with enhanced resolution portraying many anatomical landmarks and pathological signs in useful detail.

Key Words: SPECT; pinhole; bone; ankle

J Nucl Med 1998; 39:130–139
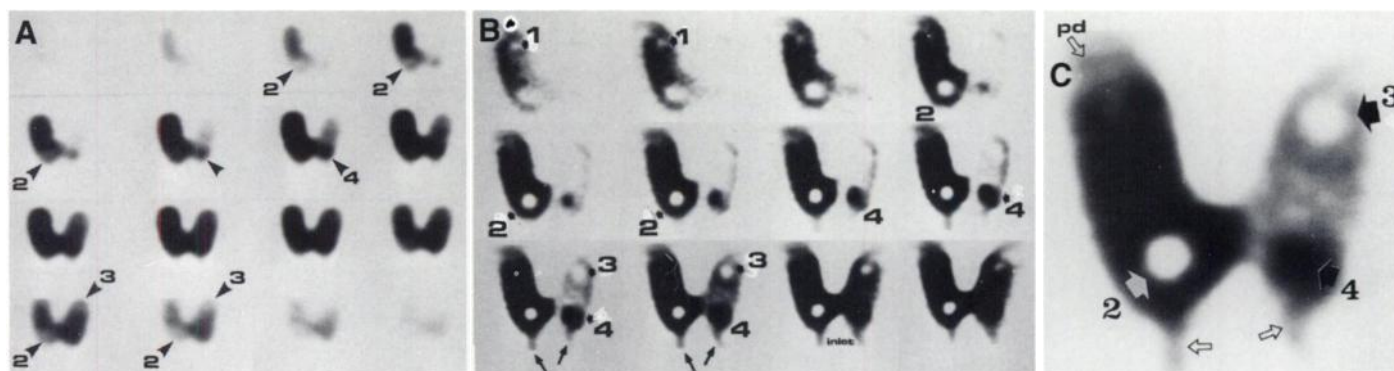
FIGURE 1. Comparison of the resolution of planar SPECT and pinhole SPECT images of thyroid phantom. (A) Planar SPECT images poorly portray the cold and hot areas (2–4) with the smallest defect in the left upper lobe not visualized. Observe the miniaturing effect. (B) Pinhole SPECT images distinctly portray all three cold areas (1–3) and a "hot" (4) area as well as the phantom contour. The injection tips are also distinctly visualized (arrows). (C) The close-up of a representative pinhole SPECT image shows how well the cold (2,3) and hot areas (4) and the injection tips are portrayed. Note the peripheral image distortion in the left upper lobe (pd).

SPECT is a nuclear imaging method that has contributed to the progress of modern cardiology, brain science, osteology and oncology. SPECT was introduced in 1963 by Kuhl and Edwards under the name "image separation radioisotope scanning" (*1*) and has since undergone continuous modification and refinement (*2–5*). SPECT images are generated from multiple-sectioned scans of an object reconstructed by using the filtered back-projection algorithm. The typical display is two-dimensional in the transaxial, coronal and sagittal planes; oblique planes can then be added. SPECT has two distinct advantages. First is the separation of disturbing radioactivities distributed in front of or behind the plane of interest. Second is contrast enhancement permitting a quantitation of photon distribution in an object (*3*). Unfortunately, however, its resolution is not improved. SPECT resolution has been shown to degrade when compared to that of the planar scan (*4*) or to be only the same at best (*5*). SPECT is not suited for the imaging of small anatomies or fine chemical alteration and has been used mostly for the imaging of a relatively large anatomical structure with prominent chemical profile alteration.

The value of the pinhole magnification technique in the study of skeletal diseases has been well-documented systemically (*6,7*), as well as in several individual bone diseases (*8–16*). Recently, the SPECT using a pinhole collimation (pinhole SPECT) to further enhance image resolution was described by Palmer and Wollner (*17*) and by Olsson and Ahlgre (*18*). The former group used a 3.3-mm pinhole collimator to magnify emission computed tomographic (ECT) images of a ^{133}Xe cylinder, ^{99m}Tc multitube phantom and a rabbit lung model, aptly naming the method "pinhole ECT," and the latter performed similar studies on ^{99m}Tc double-line phantom and human thyroid nodules. A tomographic nuclear bone imaging was attempted using cone-beam collimation (*19*). Processed with a modified software, pinhole SPECT was successfully applied recently to the diagnosis of thyroid diseases (*20*).

We have recently performed pinhole SPECT studies on a thyroid phantom and a normal and morbid ankle and hindfoot. First, pinhole SPECT resolution was assessed by comparing it with the resolution of planar SPECT images of a thyroid phantom and a normal ankle and hindfoot. As a baseline, normal pinhole SPECT anatomy of the ankle and hindfoot was worked out with a CT validation. Second, the clinical usefulness of pinhole SPECT was assessed in one patient each with a talar fracture, reflex sympathetic dystrophy syndrome (RSDS) and rheumatoid arthritis of the ankle with radiographic correlation. The resolution of pinhole SPECT was compared to that of planar SPECT and of planar pinhole scan in these ankle

diseases. We used a single-head, gamma camera system with 360° rotation feasibility that was connected to a standard software for image reconstruction using the filtered backprojection algorithm and a laser printer.

## MATERIALS AND METHODS

Thyroid Phantom

An acrylic thyroid phantom provided with three cold areas in the left upper and lower lobes and the right upper lobe and one hot area in the right lower lobe and two small injection tips was used. The phantom was filled with 185 MBq (5 mCi) ^{99m}Tc-pertechnetate solution and subjected to planar SPECT and pinhole SPECT.

Phantom Imaging Technique

The gamma camera system we used was a single-head Orbiter with a Digitrac 7500 detector with 360° rotation feasibility (Siemens Co., Germany). It was connected to an Icon data processor that enabled image reconstruction using the filtered backprojection algorithm and a Butterworth filter (Siemens Co., Germany). The planar SPECT of the phantom was performed by 360° rotation using a high-resolution, parallel-hole collimator. The collimator-to-phantom distance was 15 cm with adequate space for detector rotation and 8000 counts were accumulated per acquisition in 5 sec. A total of 64 acquisitions were made in 380 sec (5 sec/acquisition and 2 min for relocation). Images were reconstructed transaxially using the filtered backprojection method (Fig. 1A). Then, 360° pinhole SPECT was performed after replacing the parallel-hole collimator with a 4-mm pinhole collimator that was inserted into the tip of 20-cm-high shielding adapter cone (Fig. 1B,C). The scan parameters were the same as in planar SPECT except for an extension of scan time from 5 sec/acquisition to 8 sec/acquisition. Images were reconstructed using the same filtered backprojection algorithm that was provided commercially.

Clinical Studies of the Ankle and Hindfoot

Normal Ankle and Hindfoot. The baseline planar SPECT (Fig. 2A) and pinhole SPECT (Fig. 2B) were performed in the normal ankle and hindfoot of a 55-yr-old man who was referred for bone scintigraphy as a part of the clinical staging of known lung cancer. The skeletal system was normal clinically, radiographically and scintigraphically. The ankle and hindfoot were chosen because they are well separated from other body parts and provide sufficient space for 360° rotation of the detector, which was shielded with a 20-cm-high pinhole adapter cone. The ankle and hindfoot are also made up of several small irregular bones and joints that have the specific anatomical features serving as excellent morphological landmarks for an unaided eye assessment of the resolution. A matched set of sagittal CT scans of the ankle and foot was
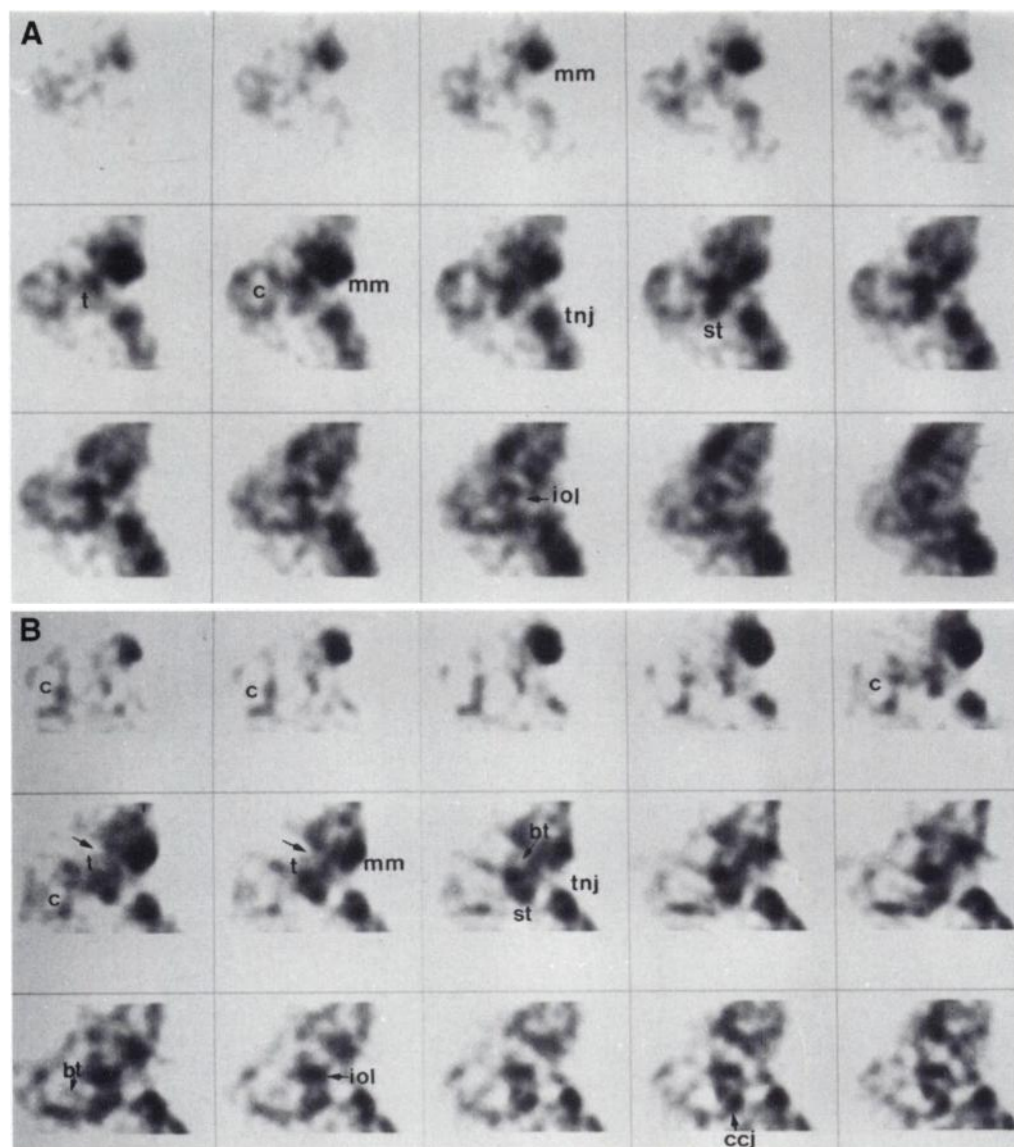
FIGURE 2. Comparison of the resolution of planar SPECT and pinhole SPECT images of a normal left ankle and hindfoot. (A) The planar sagittal SPECT images of the ankle show ill-defined and poorly separated irregular hot areas in the talus (t), the calcaneus (c), the talonavicular joint (tnj), the sustentaculum tali (st) and the interosseous ligament (iol), except in the medial malleolus (mm), which is anatomically a well separated structure. The hot areas are smudgy in appearance and the delineation of individual anatomical landmarks is less sharp. (B) In contrast, pinhole SPECT images delineate the hot areas in a discrete way satisfactorily defining small anatomies with the addition of the talocrural (arrow) and calcaneocuboid joint (ccj) (see Fig. 3). Note the sharper delineation of the cortical profile of the calcaneus (c).

obtained for reference and validation from another healthy man who had a similar radiographic foot anatomy because the patient was unwilling to have a CT scan. For an efficient correlation and reliable validation of the individual anatomy, we used the sagittal views of pinhole SPECT and CT, which were arranged in paired panels as shown in Figure 3 (A-C).

Morbid Ankle and Hindfoot. The diagnoses of three ankle diseases included an old talar fracture with deformity and secondary osteoarthritis, RSDS complicating bimalleolar fracture and rheumatoid arthritis with tenosynovitis. Diagnoses were based on laboratory tests and a plain radiograph, CT scan and MRI, where necessary, and bone scintigraphy (Figs. 4-6). The planar pinhole scan of each patient showed prominent tracer accumulation in the ankle and hindfoot, which provided sufficient radioactive counts for both planar and pinhole SPECT within a reasonably short period of time.

Planar Pinhole Scintigraphy Techniques

The planar pinhole bone scintigraphy was performed 1.5–2 hr after intravenous injection of 925 MBq (25 mCi) HDP before planar and pinhole SPECT scans using a 4-mm pinhole collimator. A total of 450–500 Kcts were accumulated over a 15–20 min period.

Techniques for Planar and Pinhole SPECT

The planar SPECT of the ankle was performed immediately after planar pinhole scan by 360° detector rotation using a high-resolution, parallel-hole collimator. The same filtered back-projection algorithm and a Butterworth filter were used for reconstruction as in the phantom study. The subject lay down in the decubitus position on a scan couch to let the medial surface of the ankle, rested on the flexed opposite knee and lower leg, be snugly placed in a slightly tilted lateral position. The collimator-to-target distance was 18 cm and 64 acquisitions were made over a period of 18 min (15 sec/acquisition and 2 min for relocation). The radioactivities accumulated were 3.5 Kcts/aquisition-14 Kcts/acquisition and the slice thickness was 2.4 mm. Pin-SPECT was performed in the same way as planar SPECT using 360° rotation of the detector that was collimated with a 4-mm pinhole and 20-cm-high adapter cone. The pinhole-to-target distance was 13–15 cm, the radioactivities accumulated were 7.5 Kcts/aquisition-8 Kcts/acquisition and the scan time was 45 min for 64 acquisitions (average 40 sec/acquisition and 2 min for relocation).

For a reliable assessment of topography, the lateral radiogram, the sagittal SPECT and CT scans were used. In the lateral and sagittal views, objects are arrayed longitudinally so that the
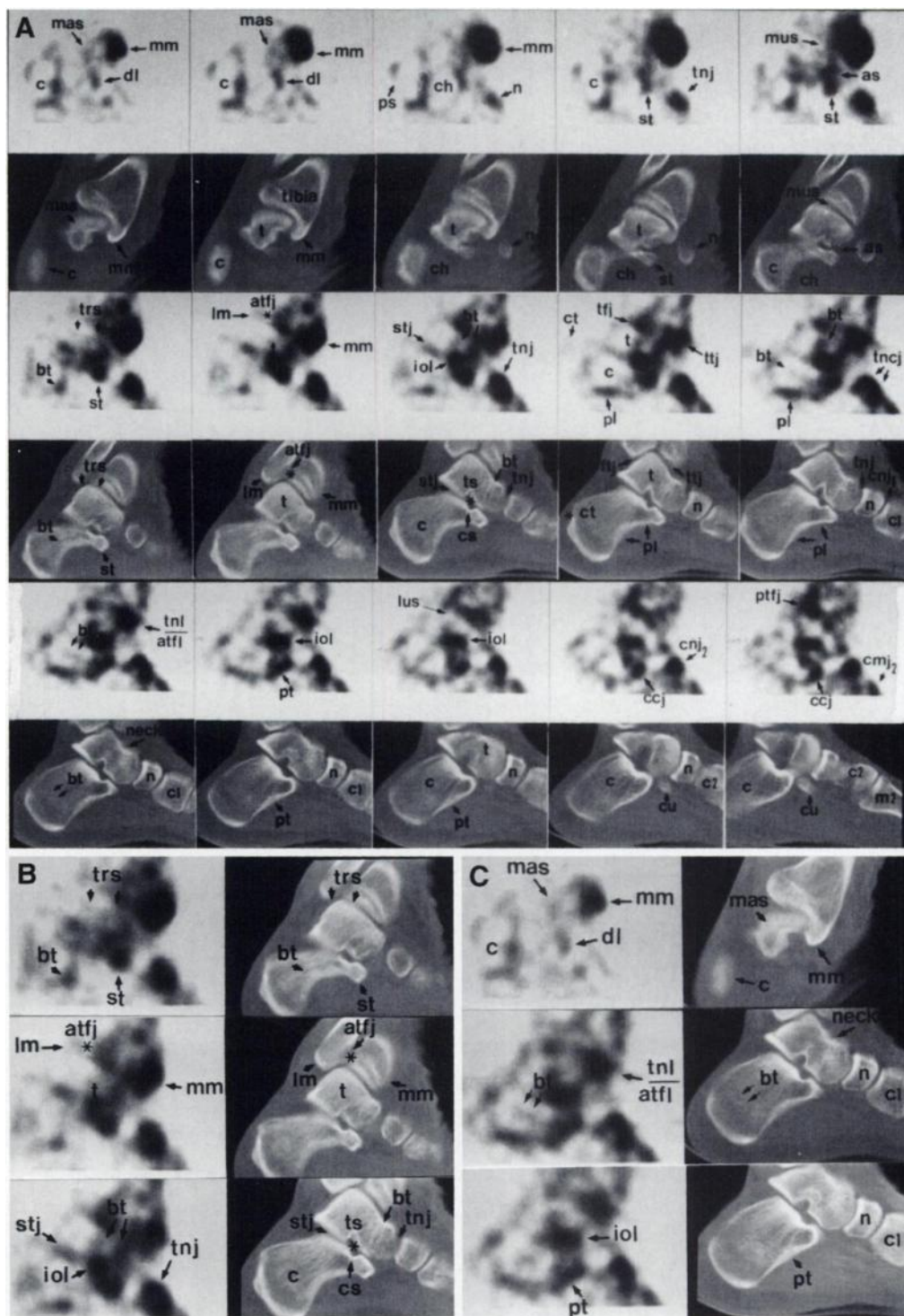
FIGURE 3. Normal sagittal pinhole SPECT anatomy of the ankle and hindfoot with CT validation. (A) Pinhole SPECT images (panels 1, 3, 5) and corresponding CT scans (Panels 2, 4, 6) of a normal ankle portray small anatomical landmarks in the ankle and hindfoot. In both pinhole SPECT and CT scans, the sectioning progresses from the medial to lateral direction and the slice thickness is 2.4 mm. The abbreviations used are spelled out in Table 1. (B) Paired close-up views of three representative pinhole SPECT and CT images clearly define anatomical landmarks including the trochlear surface (trs), condensed bone trabeculae (bt), sustentaculum tali (st), subtalar joint (stj), lateral and medial malleolus (lm and mm), talus and calcaneus (t and c) and interosseous ligament (iol). (C) Paired close-up views of the other three pinhole SPECT and CT images also clearly define the insertions of the deltoid ligament (dl), the talonavicular ligament (tnl) and the peroneal tendon (pt). In addition, the medial malleolus (mm), calcaneus (c), medial articular surface of talus (mas), navicular (n), condensed bone trabeculae (bt) and first cuneiform c_1 are portrayed.

dimension is longer (larger) and the congruency with the neighboring structure is better than in the transaxial or coronal views enabling easier recognition and more accurate identification of the individual anatomical landmarks.

Comparison of Resolution of Planar and Pinhole SPECT

An unaided visual assessment of the resolution of planar SPECT and pinhole SPECT images of the thyroid phantom was made in a semiquantitative way (Figs. 1A-C). Three senior nuclear physicians analyzed the images and the results were graded arbitrarily into poor, good and excellent according to how sharp the delineation of the phantom contour, hot and cold areas, and the injection tips were:

1. The overall resolution of the planar SPECT and pinhole SPECT images of a normal ankle and hindfoot was semiquantitatively assessed in the same way as in the thyroid phantom study and the clarity of individual anatomical landmarks was compared (Figs. 2A, B).
2. Individual anatomical landmarks were identified in the sagittal pin-SPECT images and these observations were validated against CT scans that were sliced with the same thickness of 2.4 mm as that of pinhole SPECT (Fig. 3A-C).
3. The resolution of pinhole SPECT, planar SPECT and planar pinhole scan images was compared in one case each of talar fracture with osteoarthritis (Fig. 4) and
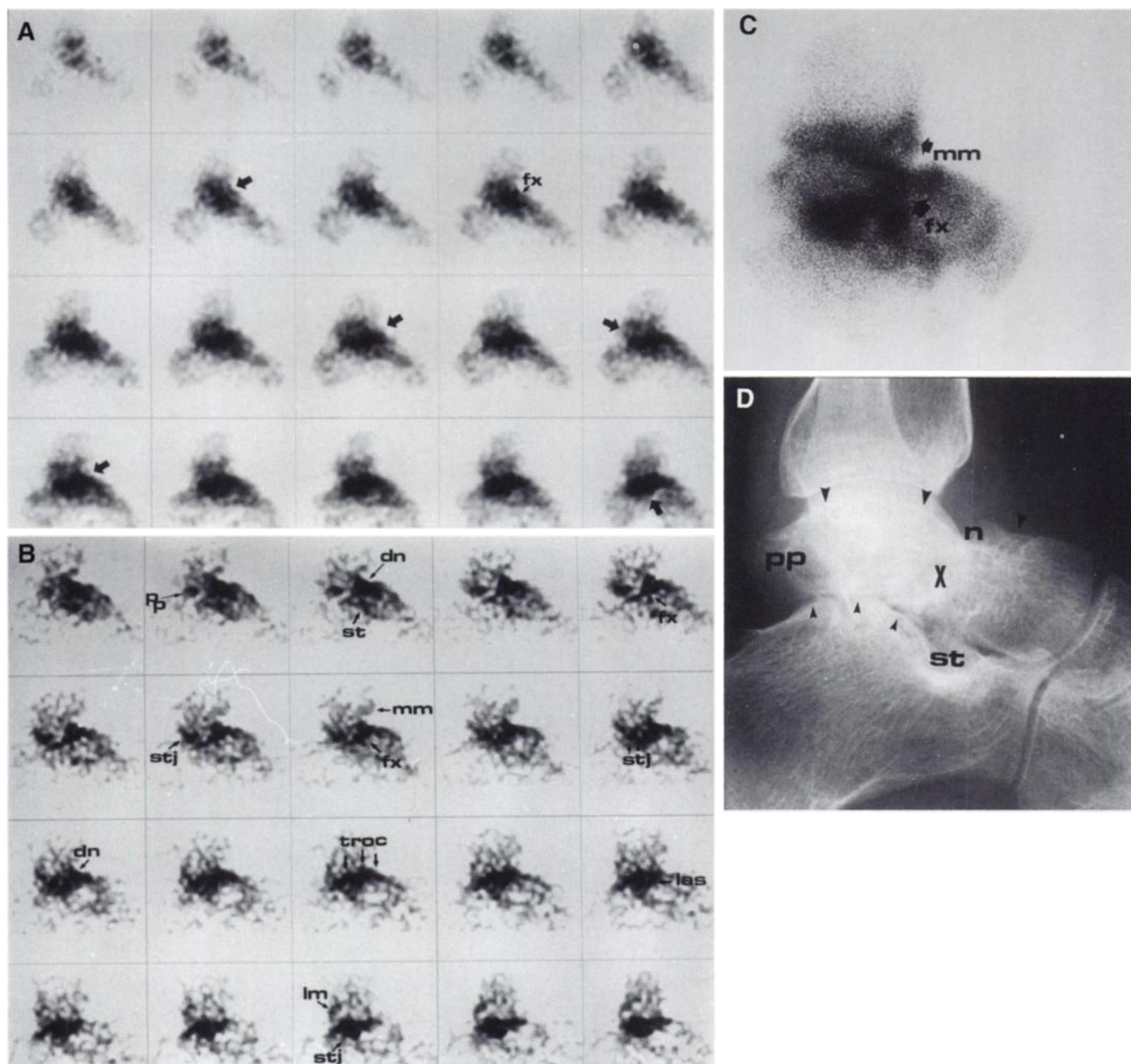
FIGURE 4. Comparison of the resolution of planar SPECT, pin-SPECT, and planar pinhole images of an old left talar fracture and osteoarthritis in the talocrural and subtalar joints with radiographic correlation. (A) The planar sagittal SPECT images show a diffuse ill-defined increased tracer accumulation in the whole ankle without localizing signs (arrow). The fracture is not well-defined (fx). (B) In contrast, the sagittal pinhole SPECT images portray sharply defined, X-shaped, intense tracer accumulation in the fracture in the central talar body (fx) with depressed neck (dn) and porotic posterior process (pp). The talus is flattened and elongated sagittally (troc and three arrows). Irregular increased tracer accumulations along the flattened trochlear surface (troc) and subtalar joint (stj) represent degenerative osteoarthritis. mm, las and lm, respectively, denote the medial malleolus, lateral articular surface of the talus and lateral malleolus. (C) The lateral planar pinhole image shows tracer accumulation in the fracture (fx), depressed neck, talocrural joint and lower talus. The separation of individual features is not so sharp as in pinhole SPECT due to overlapping. (D) The lateral radiogram shows markedly thickened trabeculae in the talar body obscuring the fracture (x). The talus is flattened, the neck depressed (n), the sustentaculum tali ill-defined (st), and the talocrural and subtalar joints are narrowed due to osteoarthritis (upper and lower arrowheads). Note the porotic posterior process (pp).

rheumatoid arthritis with tenosynovitis of the ankle (Fig. 6). In RSDS, the resolution was compared only between the pinhole SPECT and planar pinhole scan images. The resolution was assessed in terms of how distinct the delineation of the bone and articular alterations in the individual diseases were and how well they represented the pathological condition in question.

4. Pinhole SPECT signs were assessed in each disease (Figs. 4B, 5A and 6A) and the observed signs were correlated with and validated against radiography (Figs. 4D, 5C and 6C).

RESULTS

Images of the Thyroid Phantom

The resolution was poor in planar SPECT (Fig. 1A) and excellent in pinhole SPECT (Figs. 1B, C). Planar SPECT could not clearly define individual cold and hot areas. The smallest cold area in the left upper lobe and the injection tips were virtually indistinguishable. In contrast, pinhole SPECT could sharply define the phantom contour with two injection tips as well as three cold and one hot areas. There was
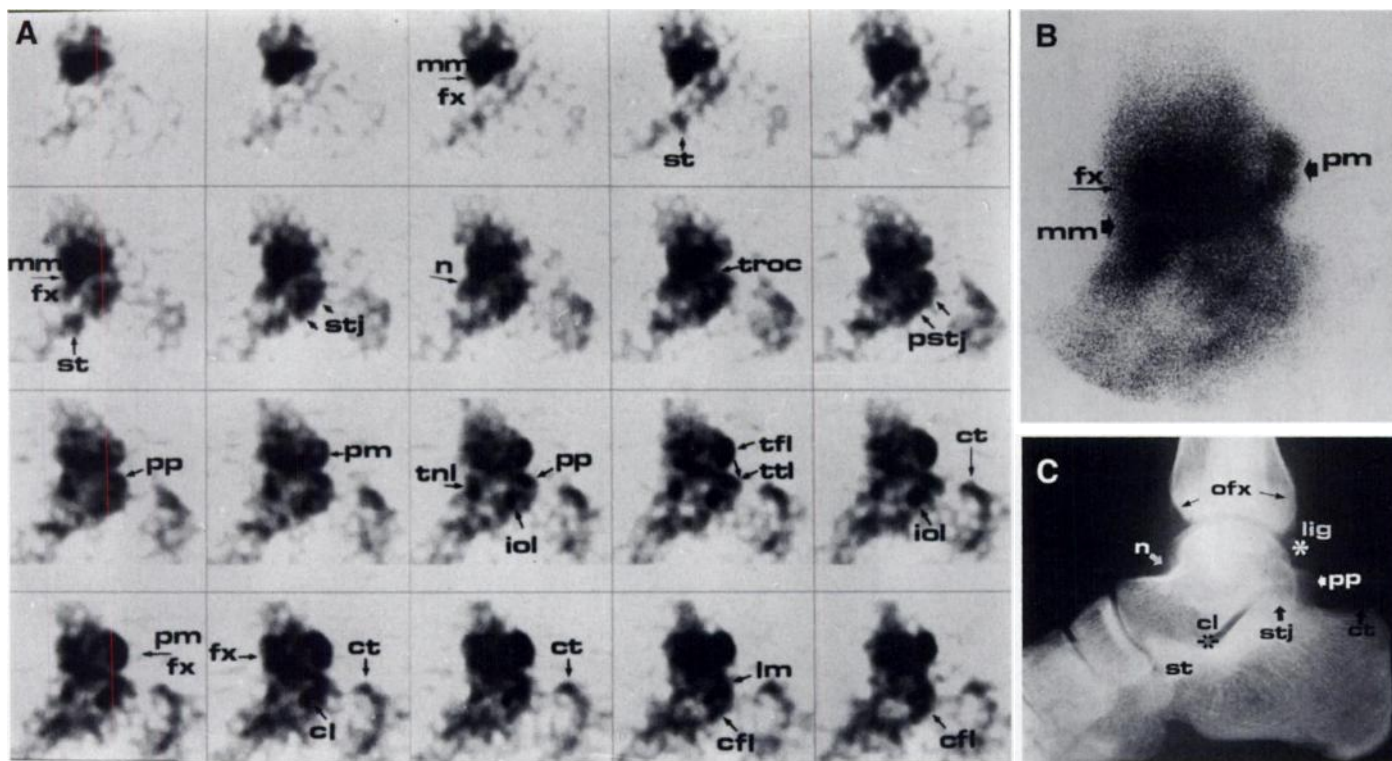
FIGURE 5. Ovoid and spotty hot areas in the ligamentous and tendinous insertions in pinhole SPECT images of RSDS, planar pinhole scan comparison, and radiographic correlation. (A) The sagittal pinhole SPECT images of the right ankle show many characteristic discrete ovoid and spotty hot areas in insertions of the talonavicular ligament at talar neck (tnl at n), posterior tibiotalar and talofibular ligaments at posterior malleolus and posterior talar process (ttl, tfl at pm, pp), interosseous and cervical ligaments at subtalar bone (iol, cl at stj, pstj) and calcaneofibular ligament at lateral malleolus (cfl at lm) and the lateral part of calcaneus (last two frames in bottom panel). The calcanean tendon insertion at posterior calcanean surface tip (ct) and fracture in medial malleolus, which is responsible for RSDS in this patient, concentrate tracer intensely (mm, fx). (B) The lateral planar pinhole image shows diffuse tracer accumulation in the ankle joint, medial and posterior malleoli (mm, pm), and fracture (fx). Separation of anatomy is insufficient due to overlapping and the ovoid and spotty hot areas are not visualized. (C) Lateral radiogram shows multiple blotchy areas of subcortical bone resorption in tendinous insertions at talar neck (n), posterior malleolus (lig), posterior process (pp), subtalar joint bone (stj), sustentaculum tali (st) and posterior calcanean surface tip (ct). Old bimalleolar fracture is also shown (ofx).

considerable image distortion in the extreme periphery of the field-of-view due to the inherent hardware problems of the detector system.

Images of Normal Ankle and Hindfoot

The comparison of the resolution of planar SPECT (Fig. 2A) and pinhole SPECT images (Figs. 2B and 3A-C) of a normal ankle and hindfoot showed the resolution of the latter SPECT to be significantly better. Bone and joint anatomy were better defined in the pin-SPECT images than in the planar SPECT images and so the identification, with pin-SPECT, of individual anatomical landmarks was much easier and more accurate. In addition, pin-SPECT was able to delineate the subtle metabolically-active anatomical landmarks such as the tendinous and ligamentous insertions and condensed trabeculae in the weight-bearing axes of the talus and calcaneus (Figs. 2B and 3A-C).

Pinhole SPECT was able to delineate all major anatomical landmarks in the ankle and hindfoot (Fig. 3A, panels 1, 3, 5), and each of the landmarks was closely correlated with, and validated against, the CT scan (Fig. 3A, panels 2, 4, 6). The anatomical landmarks observed and validated were as shown in Table 1. It was possible to identify the medial and lateral malleoli along with the talofibular joint, talocrural joint, subtalar joint, sustentaculum tali, talar neck and talonavicular joint (Fig. 3B). The insertions of the talofibular ligament, talonavicular ligament, deltoid ligament, cervical ligament, interosseous ligament and peroneal tendon were also clearly identified (Fig. 3C). In the normal ankle, the joints accumulated tracer more avidly than the tendious or ligamentous insertions. This relationship became reversed in RSDS. The thickened trabeculae in

the weight-bearing axes of the talus and calcaneus were portrayed as small, band-like intraosseous tracer accumulations reflecting their increased metabolic activity (Fig. 3B, panel 3; Fig. 3C, panel 2). To identify the small anatomical landmarks in the hollow medial aspect (Fig. 3A, top panel; Fig. 3C, panel 1) and rough lateral surface of the talus and calcaneus, much greater scrutiny was required.

Images of Morbid Ankles and Hindfeet

Comparing the resolution of planar SPECT, pinhole SPECT and planar pinhole scan in talar fracture, RSDS and rheumatoid arthritis showed significant differences in the demonstrability of pathological alterations. The planar SPECT of the talar fracture showed an ill-defined increased tracer accumulation in the ankle without specific or localizing signs (Fig. 4A). However, pinhole SPECT showed a distinct X-shape tracer accumulation in the fracture (Fig. 4B). The talar body collapse, the talar neck depression and the secondary osteoarthritis in the talocrural and subtalar joints were also clearly delineated. All such pinhole SPECT alterations were closely correlated with the radiographic alterations (Fig. 4D). Somewhat similar differences were observed between the resolution of planar SPECT and of pinhole SPECT in rheumatoid arthritis. No comparison study was done in RSDS.

The resolution of the pinhole SPECT and the planar pinhole scan in all three diseases also differed significantly (Figs. 4C, 5B and 6B). The resolution of the planar pinhole scan showed well-delineated major anatomical landmarks, but there was overlapping. In both RSDS and rheumatoid arthritis, the planar pinhole scan showed diffusely increased tracer accumulation in

the ankle obliterating the talocrural joint. However, pinhole SPECT showed a different tracer accumulation pattern. The pinhole SPECT in RSDS was characterized by many small discrete ovoid and spotty areas of intense tracer accumulation in the tendinous and ligamentous insertions and the subcortical bone resorption (Fig. 5A). The pinhole SPECT in rheumatoid arthritis was characterized by diffused tracer accumulation in the intercommunicating synovial joints of the ankle. In the talar fracture, both the pinhole SPECT and planar pinhole scan portrayed fracture and talar body collapse equally well, but the osteoarthritis in the trochlear surface and the subtalar articular bone was more distinctly portrayed in pinhole SPECT (Figs. 4B, C).

The assessment of the pinhole SPECT manifestations of the three ankle diseases showed several interesting signs that appeared to be specific to the disease in question.

SAMPLE CASES

*Case 1.*This case was a 19-yr-old man with a 10-mo-old left talar fracture with body collapse and neck depression as well as secondary osteoarthritis in the talocrural and subtalar joints (Fig. 4D). The pinhole SPECT clearly portrayed an X-shaped fracture involving the talar body that was collapsed and depressed in the neck. Osteoarthritic alterations were also distinctly visualized (Fig. 4B). The planar SPECT showed generalized tracer accumulation in the whole ankle and visualized neither a fracture nor osteoarthritic joints (Fig. 4A). The

resolution of the planar pinhole scan was higher than the planar SPECT (Fig. 4C), but it was lower than the pinhole SPECT. Arthritic alterations in the talocrural and subtalar joints and fracture were most clearly shown in pinhole SPECT.

*Case 2.*This case was a 29-yr-old man with RSDS that was related to a bimalleolar fracture in the right ankle. Radiography showed an old fracture with several small, blotchy subcortical bone resorption areas in the regional bones (Fig. 5C). The pinhole SPECT showed prominent tracer accumulation in the bimalleolar fracture that underlay RSDS. Most importantly, multiple discrete ovoid and spotty hot areas were portrayed at the insertions of the talofibular, tibiotalar, cervical and talonavicular ligaments as well as at the calcanean tendon where subcortical bone resorption was shown radiographically (Fig. 5A). The latter finding probably denotes "the dramatic bone resorption mediated by vasoactive intestinal peptide liberated from sympathetic nerve fibers in RSDS" (*25*). In contrast, however, the planar pinhole scan showed tracer accumulation to be simply diffuse with no distinguishing or localizing features (Fig. 5B). The ovoid and spotty hot areas shown in pinhole SPECT, at the insertions of the tendon and ligament, were not portrayed in the planar pinhole scan. Unlike in the normal pinhole SPECT, the tracer accumulation pattern in RSDS was reversed showing a higher tracer accumulation in the morbid ligamentous and tendinous insertions and not in the articulations.

*Case 3.*This case was a 53-yr-old woman with acute recurrent rheumatoid arthritis of her left ankle and articular narrowing and periarticular soft tissue swelling (Fig. 6C). Planar SPECT showed increased diffuse tracer accumulation in the ankle without localizing signs. However, pinhole SPECT showed intense tracer accumulation distributed in the narrowed articular spaces of the tibiofibular, talocrural, subtalar, talonaviculocuneiform and calcaneocuboid joints (Fig. 6A). Such a tracer accumulation pattern appears to be characteristic of rheumatoid arthritis which affects synovial joints in a diffuse way. Intense tracer accumulation also took place in the blotchy, subchondral bone erosions in the medial malleolus and talar neck. There was a bar-like tracer accumulation in the distal fibula that was connected inferiorly to the subtalar joint and the lateral aspect of the calcaneus (Fig. 6A). This indicates calcaneofibular tenosynovitis, which is a well-known complication of rheumatoid arthritis.
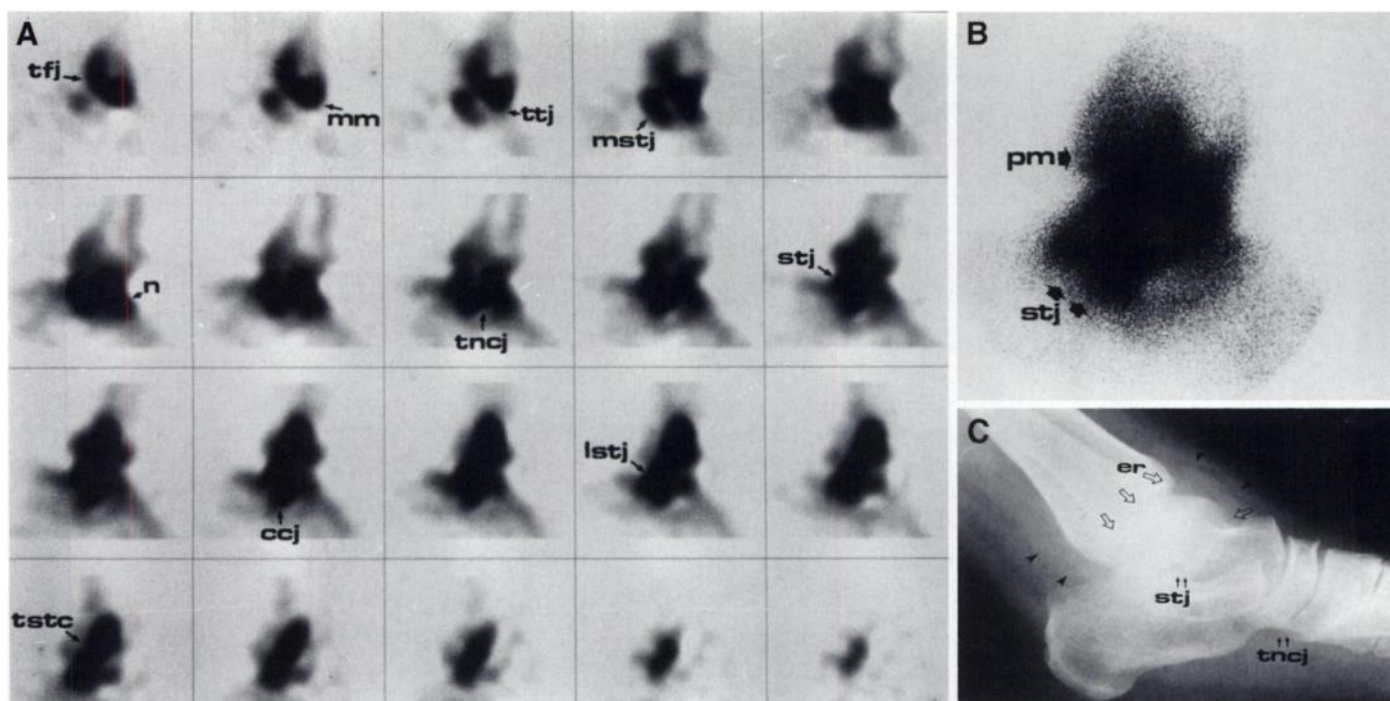
The planar pinhole scan in rheumatoid arthritis showed a diffuse tracer accumulation in the whole ankle without a localizing feature as shown in RSDS (Figs. 5B and 6B). In pinhole SPECT, the tracer accumulation was typically diffuse in rheumatoid arthritis, but it was spotty and localizing in RSDS.

DISCUSSION

The general premise that a high-quality image is essential to reliable imaging diagnosis also applies to nuclear bone imaging. Since the original diagnostic uses for nuclear bone imaging were established in 1961 by Fleming et al. (*21*), nuclear bone imaging has been valued for its sensitivity in the detection of occult fracture, cryptic infection and early malignant metastasis. It demonstrates low specificity because of miniaturing and overlapping of the display images. As remedies, the planar SPECT, magnification techniques and some other modified techniques have been introduced.

Planar SPECT has two advantages. The first is the separation of the radioactivities that are distributed in front of or behind the plane of interest, and the second is the contrast enhancement (*3*). The specificity is not much improved. The resolution of SPECT is either degraded compared to the planar scan (*4*) or

FIGURE 6. The characteristic pinhole SPECT manifestation of acute rheumatoid arthritis and planar pinhole scan comparison and radiographic correlation. (A) The sagittal pinhole SPECT images of left ankle portray intense tracer accumulation in the narrowed ankle articulations including the talofibular and talotibial joints (tfj, ttj), talonaviculocuneiform joint (tncj), medial, lateral and posterior subtalar joints (mstj, lstj, stj) and calcaneocuboid joint (ccj). Marked tracer accumulation is seen in eroded medial malleolus (mm) and calcaneofibular tenosynovitis with a tendosubtalar connection (tstc). (B) Lateral planar pinhole scan shows intense tracer accumulation in ankle without any distinguishing features. Posterior malleolus (pm) and subtalar joint (stj) are discernible. (C) Lateral radiogram shows diffuse articular narrowing (open arrows), periarticular swelling (arrowheads) and subchondral erosions in the talocrural joint (er), talar neck (single open arrow), subtalar joint (stj) and the talonaviculocuneiform joint (tncj).

equal to it at best (5). We could also confirm that the resolution of planar SPECT is lower than that of the simple planar images (22,23). The low resolution of planar SPECT is related to the characteristics of the parallel hole collimator that is designed to enhance the sensitivity at the cost of resolution. A finite cutoff frequency of the reconstruction filter, limited intervals of angular sampling and display matrix sizes also affect the resolution (24). The reduced display matrix size contributes to the lowering of the resolution because of the concealment of fine morphologic and metabolic information. The planar SPECT image displayed on a small matrix is unsuitable for portraying small objects and fine chemical alterations. This examination is more typically used to study larger bones such as the spine, hip and knee joints (4).

The value of the pinhole magnification technique to study skeletal diseases has been described systemically (6,7) as well as in many individual bone and joint diseases (8–16). Enhancing the resolution of SPECT with pinhole collimation was introduced by Palmer and Wollner (17) and by Ollson and Ahlgren (18). The former group used a 3.3-mm pinhole collimator to magnify ECT images of ^{133}Xe cylinder, ^{99m}Tc multitube phantom, and a rabbit lung model, aptly naming the technique "pinhole ECT," and the latter performed a similar study on ^{99m}Tc double-line phantom and human thyroid nodules. An attempt has also been made at using a cone-beam collimator as a tool of tomographic nuclear bone imaging (19). The pinhole SPECT, processed with a modified software, diagnosed some thyroid diseases (20). We performed a series of pinhole SPECT studies utilizing a standard reconstruction alogrithm and a Butterworth filter on a thyroid phantom and normal and morbid ankles observing the enhanced resolution and potent applicability to the diagnosis of important ankle diseases.

Our experimental study on a thyroid phantom showed the resolution of planar SPECT (Fig. 1A) to be rather low compared to that of pinhole SPECT (Figs. 1B,C). Planar SPECT was able to portray the large cold and hot areas of the phantom but not small cold ones. The injection tips were not visualized either. However, pinhole SPECT could clearly portray all three cold and one hot areas and the small injection tips (Fig. 1B,C). There was no penumbra, but significant image distortion occurred in the periphery, which will require development of new software and hardware. The clinical studies included: (a) comparison of the resolution of planar and pinhole SPECT of a normal ankle and hindfoot; (b) assessment of pinhole SPECT anatomy of a normal ankle and hindfoot with CT validation; (c) sorting of diagnostic pinhole SPECT signs in ankle diseases with radiographic correlation; and (d) comparison of the resolution of pinhole SPECT and planar pinhole scan in ankle diseases. As in the phantom test, the resolution of pinhole SPECT was higher than that of planar SPECT delineating anatomy and morbid findings more sharply due to improved two-point discrimination (Figs. 2A,B and 4A,B). Pinhole SPECT could portray most of the important anatomical landmarks (Fig. 3A, panels 1, 3, 5) and each of them was correlated with and validated against CT scans (Fig. 3A, panels 2, 4, 6). We could identify the medial and lateral malleoli, talofibular joint, talocrural joint, subtalar joint, sustentaculum tali, talar neck and talonavicular joint (Fig. 3B) and the insertions of the tibiotalar, talofibular, talonavicular, cervical, interosseous and deltoid ligaments as well as the peroneal tendon (Fig. 3C).The reinforced or condensed trabeculae in the weight-bearing axes of the talus and calcaneus were imaged as a small bar-like increased tracer accumulation reflecting increased metabolic activity (Fig. 3B, panel 3 and Fig. 3C, panel 2). The portrayal of such a subtle anatomico-chemical profile is one outstanding feasture of pinhole SPECT. Assessing the hollow medial and roughened lateral aspects of

the talus and calcaneus required greater scrutiny (Fig. 3A, top and bottom panels and Fig. 3C, top panel).

The diagnostic application of pinhole SPECT to talar fracture, RSDS and rheumatoid arthritis of the ankle was also useful. The pinhole SPECT images in these diseases showed several diagnostic signs. The old talar fracture in Case 1 was sharply delineated as an X-shape tracer accumulation in the talar body and neck portraying both the morphological and metabolic state of the fracture 10 mo after the initial incident (Fig. 4B). The talus was flattened and elongated sagitally and the trochlear surface and subtalar bone were covered with a sharply defined crest-like tracer accumulation denoting secondary osteoarthritis. Both the planar SPECT and radiography failed to sharply delineate the fracture and osteoarthritis (Figs. 4A,D). The planar pinhole scan also portrayed all these features, but each feature was not sharply defined as in pinhole SPECT because of overlapping (Fig. 4C). RSDS in Case 2 showed intense tracer accumulation in the bimalleolar fracture that underlay RSDS in this patient. Many discrete ovoid hot areas were shown in the peripheries and edges of the talus and calcaneus (Fig. 5A). Topographically, the hot areas matched with radiographic blotchy, subcortical bone resorption in the talus and calcaneus (Fig. 5C) which, in turn, coincided with regional tendious and ligamentous insertions (Fig. 5A,).The discrete ovoid hot areas indicate the specific sites in the corticoperiosteal junction where the sympathetic nerve fibers containing vasoactive intestinal peptide were innervated. These nerve fibers have been experimentally shown to stimulate osteoclastic activities resulting in dramatic focal bone resportion as observed in this case (25). The pinhole SPECT in acute recurrent rheumatoid arthritis in Case 3 portrayed a tracer accumulation throughout the entire peritalar joints including the talocrural, talofibular, talonaviculocuboid and subtalar joints, which were narrowed and communicating each other (Fig. 6A). The pinhole SPECT alterations were well correlated with radiographic alterations (Fig. 6B). An intense bar-like tracer accumulation occurred in the calcaneofibular tendon that connected the fibular tip to the lateral aspect of the calcaneus overpassing the posterior subtalar joint. Such a tendoarticular connection has been shown in rheumatic tenosynovitis in the ankle using contrast synoviography (26). Characteristically, the articular and tendious tracer accumulation in acute rheumatoid arthritis was intense and diffuse obliterating the regional anatomy. This kind of scan feature sharply contrasted with RSDS and fracture with osteoarthritis whose pinhole SPECT alterations tended to be discrete and localizing (Figs. 4B and 5A).

In Cases 2 and 3, the comparison of the resolution of pinhole SPECT and planar pinhole scan showed notable differences. In both cases, the planar pinhole scan showed only intense diffuse tracer accumulation in the ankle without differential features (Figs. 5B and 6B). In contrast, however, pinhole SPECT, in RSDS, portrayed multiple discrete ovoid and spotty hot areas (Fig. 5A), and, in acute recurrent rheumatoid arthritis, a bizarre intercommunicating articular tracer accumulation (Fig. 6A).

CONCLUSION

The resolution or imaging performance of pinhole SPECT was remarkable in our studies that included a thyroid phantom test, the assessment of a pinhole SPECT anatomy of a normal ankle and hindfoot and clinical diagnostic application to some ankle diseases. Despite image distortion that occurred in the extreme periphery of the field-of-view, pinhole SPECT could sharply portray the phantom profile, cold and hot areas and the injection tips. The topographic portrayal of the ankle and hindfoot was clear so that all small, important anatomical

landmarks were identified. The small areas of condensed trabeculae in the weight-bearing axes in the talus and calcaneus were delineated among the unstressed bones. The pinhole SPECT portrayal of the talar fracture with secondary osteoarthritis, the peculiar blotchy subcortical bone resorption in the ligamental and tendinous insertions in RSDS and the intercommunicating synovial articular inflammation and related tenosynovitis in rheumatoid arthritis was unique. The information revealed by pinhole SPECT was not only morphological but metabolic.The location, appearance and intensity of the tracer accumulated in the fracture, RSDS and rheumatoid arthritis simultaneously denoted both anatomical and metabolic states of the pathological process in question. The comparison with planar pinhole scan in the morbid ankle showed pinhole SPECT generates nuclear images with remarkably improved two-point separation. With the development of new software programs for improved image processing and hardware design for higher sensitivity and unlimited range of detector rotation, pinhole SPECT will become a potent nuclear imaging modality.

REFERENCES

1. Kuhl DE, Edwards RQ. Image separation radioisotope scanning. *Radiology* 1963;80: 653–662.
2. Kuhl DE, Edwards RQ. Cylindrical and section radioisotope scanning of the liver and brain. *Radiology* 1964;83:926–936.
3. Jaszczak RJ, Murphy PH, Huard D, Burdine JA. Radionuclide emission computed tomography of the head with ^{99m}Tc and a scintillation camera. *J Nucl Med* 1977;18:373–380.
4. Collier BD. Orthopaedic applications of single photon emission computed tomographic bone scanning. In: Fogelman I, ed. *Bone scanning in clinical practice*. London: Springer-Verlag; 1989:175–187.
5. Groch MW, Erwin WD, Bieszk JA. Single photon emission computed tomography. In: Treves ST, ed. *Pediatric nuclear medicine*, 2nd ed. New York: Springer-Verlag; 1995:33–87.
6. Bahk YW. *Combined scintigraphic and radiographic diagnosis of bone and joint disease*. Heidelberg, New York: Springer-Verlag; 1994.
7. Treves ST, Connolly LP, Kirkpatrick JA, Packard AB, Roach P, Jaramillo D. Bone. In: Treves ST, ed. *Pediatric nuclear medicine*, 2nd ed. New York: Springer-Verlag; 1995:233–301.
8. Bahk YW, Kim OH, Chung SK. Pinhole collimator scintigraphy in the differential diagnosis of metastasis, fracture, and infections of the spine. *J Nucl Med* 1987;28: 447–451.
9. Bahk YW, Chung SK, Kim SH. Pinhole scintigraphic manifestations of sternocostoclavicular hyperostosis. *Korean J Nucl Med* 1992;26:155–159.
10. Kim JY, Chung SK, Park YH, Kim SH, Bahk YW. Pinhole bone scintigraphic appearance of osteoid osteoma. *Korean J Nucl Med* 1992;26:160–163.
11. Kim SH, Bahk YW, Chung SK, Shinn KS. Pinhole scintigraphic appearance of infantile cortical hyperostosis. "Bumpy" segmental tracer uptake. *Korean J Nucl Med* 1993;27:319–320.
12. Yang WJ, Bahk YW, Chung SK, Choi KH, Jo KH, Jee MK. Pinhole skeletal scintigraphic manifestations of Tietze's disease. *Eur J Nucl Med* 1994;21:947–952.
13. Bahk YW, Park YH, Chung SK, Kim SH, Shinn KS. Pinhole scintigraphic sign of chondromalacia patellae in older subjects: a prospective assessment with differential diagnosis. *J Nucl Med* 1994;35:855–862.
14. Bahk YW, Park YH, Chung SK, Chi JG. Bone pathologic correlation of multimodality imaging in Paget's disease. *J Nucl Med* 1995;36:1421–1426.
15. Bahk YW. Pinhole scanning in tumors and tumorous conditions of bone: a new imaging approach to skeletal oncology. *J Orthop Sci* 1996;1:70–89.
16. Conway JJ. Radionuclide evaluation of Legg-Calvé-Perthes disease. In: Treves ST, ed. *Pediatric nuclear medicine*, 2nd ed. New York: Springer-Verlag; 1995:302–315.
17. Palmer J, Wollmer P. Pinhole emission computed tomography: method and experimental evaluation. *Phys Med Biol* 1990;35:339–350.
18. Olsson LE, Ahlgren L. Tomographic scintigraphy using a pinhole collimator and a rotating gamma camera. *Nuklearmedizin* 1990;29:47–50.
19. Cooper JA, Mahmood MM, Smith HS, McCandless BK. Tomographic imaging of the distal extremities using cone-beam collimation. *J Nucl Med* 1994;35:914–917.
20. Wanet PM, Sand A, Abramovici J. Physical and clinical evaluation of high-resolution thyroid pinhole tomography. *J Nucl Med* 1996;37:2017–2020.

21. Fleming WH, McIlraith JD, King R. Photoscanning of the bone lesions utilizing strontium 85. *Radiology* 1961;77:635–636.

22. Bahk YW. Pinhole scan and single photon emission computed tomography in the diagnosis of bone and joint disease. *Proceedings of an international symposium on tomography in nuclear medicine.* Vienna: IAEA; 1995:197–214.

23. Bahk YW. Pinhole scan vs SPECT in the diagnosis of bone and joint disease: an improved scan delineation of structure and physiochemical profile. In: Torizuka K, ed. *Syllabus of educational lecture.* Kyoto: The Sixth Asia and Oceania Congress of Nuclear Medicine and Biology; 1996:1–8.

24. Sorenson JA, Phelps ME. Nuclear medicine tomography: principles. In: Sorenson JA, Phelps ME, eds. *Physics in nuclear medicine,* 2nd ed. Philadelphia: WB Saunders; 1987:391–423.

25. Hohmann EL, Elde RP, Rysavy JA, Einzig S, Gebhard RL. Innervation of periosteum and bone by sympathetic vasoactive intestinal peptide-containing nerve fibers. *Science* 1986;232:868–871.

26. Hug G, Dixon STJ. Ankle joint synoviography in rheumatoid arthritis. *Ann Rheum Dis* 1977;36:532–539.